Deformed coordinate-space Hartree-Fock-Bogoliubov approach to weakly bound nuclei and large deformations

J. C. Pei,[1,2,3] M. V. Stoitsov,[2,3,4] G. I. Fann,[3] W. Nazarewicz,[2,3,5] N. Schunck,[2,3] and F. R. Xu[6]
[1]*Joint Institute for Heavy Ion Research, Oak Ridge, Tennessee 37831, USA*
[2]*Department of Physics and Astronomy, University of Tennessee, Knoxville, Tennessee 37996, USA*
[3]*Oak Ridge National Laboratory, P.O. Box 2008, Oak Ridge, Tennessee 37831, USA*
[4]*Institute of Nuclear Research and Nuclear Energy, Bulgarian Academy of Sciences, Sofia, Bulgaria*
[5]*Institute of Theoretical Physics, Warsaw University, ul.Hoża 69, PL-00681 Warsaw, Poland*
[6]*State Key Laboratory of Nuclear Physics and Technology, School of Physics, Peking University Beijing 100871, People's Republic of China*
(Received 18 July 2008; revised manuscript received 16 October 2008; published 15 December 2008)

The coordinate-space formulation of the Hartree-Fock-Bogoliubov (HFB) method enables the self-consistent treatment of mean field and pairing in weakly bound systems whose properties are affected by the particle continuum space. Of particular interest are neutron-rich, deformed drip-line nuclei, which can exhibit novel properties associated with neutron skin. To describe such systems theoretically, we developed an accurate two-dimensional lattice Skyrme-HFB solver HFB-AX based on basis (or B)-splines. Compared to previous implementations, ours incorporated a number of improvements aimed at boosting the solver's performance. These include the explicit imposition of axiality and space inversion, use of the modified Broyden method to solve self-consistent equations, and a partial parallelization of the code. HFB-AX has been compared with other HFB codes, both spherical and deformed, and the accuracy of the B-spline expansion was tested by employing the multiresolution wavelet method. Illustrative calculations are carried out for stable and weakly bound nuclei at spherical and very deformed shapes, including constrained fission pathways. In addition to providing new physics insights, HFB-AX can serve as a useful tool to assess the reliability and applicability of coordinate-space and configuration-space HFB frameworks, both existing and in development.

DOI: 10.1103/PhysRevC.78.064306 PACS number(s): 21.60.Jz, 21.10.−k, 02.70.−c, 31.15.ej

I. INTRODUCTION

An important new aspect of theoretical nuclear structure research is the development of a coherent theoretical framework aimed at the microscopic description of nuclear many-body systems and capable of extrapolating into unknown regions. An important component in the theoretical landscape, and a crucial part of the theory road map [1,2], is the nuclear density functional theory (DFT) in the formulation of Kohn and Sham [3]. Since the majority of nuclei in their ground states are superconductors, pairing correlations have to be taken into account. The resulting HFB or Bogoliubov-de Gennes equations can be viewed as the generalized Kohn-Sham equations of the standard DFT. The main ingredient of the nuclear DFT [4,5] is the energy density functional that depends on proton and neutron densities and currents, as well as pairing densities representing correlated nucleonic pairs [6].

The unique structural factor that determines many properties of weakly bound nuclei is the closeness of the particle continuum. While the nuclear densities of bound nuclei eventually vanish at large distances, the wave functions of positive-energy states do not decay outside the nuclear volume, and this can be a source of significant theoretical difficulties. This problem is naturally overcome in the HFB method with a realistic pairing interaction in which the coupling of bound states to the particle continuum is correctly taken into account.

One commonly used way of solving the self-consistent HFB equations of the nuclear DFT is via iterative schemes involving direct diagonalization of the HFB Hamiltonian. Another approach is to minimize the energy functional by means of the gradient method. Regardless of the scheme, however, the associated computational effort is largely dictated by the self-consistent symmetries imposed and/or the number of quasiparticle states included. The advent of teraflop computers makes large-scale DFT calculations, involving millions of nuclear states, feasible. However, to take advantage of multicore/multiprocessor architectures, new-generation HFB solvers have to be developed.

The HFB problem is often formulated in the configuration space by expanding the quasiparticle states of HFB in a suitable single-particle basis, such as the harmonic oscillator (HO) basis [7]. This method is very efficient and has been applied successfully in large-scale calculations of nuclear properties [8]. However, the use of the HO basis is questionable in the limit of both weak binding and very large deformations, both requiring the use of unrealistically large configuration spaces to guarantee convergence. In both situations, the coordinate-space approach to the HFB problem [9,10] is superior.

A number of coordinate-space techniques have been developed over the years, and their performance strongly depends on the size and symmetries of the spatial mesh employed [11–13]. The one-dimensional (1D) HFBRAD finite-difference code has been developed as a standard tool for HFB calculations in spherical nuclei [14]. While limited to the radial coordinate only, HFBRAD allows very precise calculations, as the mesh step can be taken very low. The recently developed parallel two-dimensional code, HFB-2D-LATTICE [15–17], is based on

B-splines; it can treat axially deformed nuclei, including those with reflection-asymmetric shapes. A coordinate-space HFB code based on a finite-difference method with a 2D equidistant mesh has also been published very recently [18]. This code also describes axial nuclei and breaks mirror symmetry.

Solving the HFB equations in a three-dimensional (3D) coordinate space is not a simple task; hence, very few such solvers are available. The EV8 code solves the Hartree-Fock plus BCS equations for Skyrme-type functionals via a discretization of the individual wave functions on a 3D Cartesian mesh and the imaginary time method [19]. Three symmetry planes are assumed, and only the eigenfunctions corresponding to the lowest eigenvalues are evaluated. Its HFB extension, using a two-basis method, has been developed in Ref. [12]. The rapid growth of the number of positive-energy HF states representing the discretized continuum with the size of the mesh prohibits the use of large pairing windows in this method; hence the applicability of this code is limited to well-bound nuclei. Another useful technique that can be used to solve the 3D HFB problem in coordinate space is the canonical-basis decomposition [20]. In this method, however, the HFB Hamiltonian becomes state-dependent, and the momentum-dependent pairing interaction is required to circumvent the so-called point collapse problem [20]. Finally, it is worth noting that developments based on novel concepts are underway, such as a general-purpose 3D HFB solver based on multi-resolution analysis and wavelet expansion. This technique has been successfully applied in quantum chemistry and is currently being adapted to nuclear structure [21,22].

The main objective of this paper is to develop a reliable, accurate, and fast HFB axial solver based on the B-spline mapping technique that could be used to perform large-scale calculations of nuclear properties and to produce reference (or benchmark) results to test future 3D HFB solvers. One of the requirements is that the code can be applied to neutron-rich, weakly bound nuclei (where the accurate description of densities and fields at large distances is essential) and to symmetric fission pathways of the heaviest elements (where the shape elongations and the corresponding spatial dimensions are large). Such a scheme has already been implemented in the HFB-2D-LATTICE by the Vanderbilt group [15–17]. An attractive feature of the HFB-2D-LATTICE is that by taking high-order B-splines, one guarantees the correct representation of derivative operators on the spatial lattice [11]. However, the usefulness of the HFB-2D-LATTICE is strongly limited by its slow execution time and large memory requirements when it comes to large-scale calculations. Moreover, a systematic comparison of the HFB-2D-LATTICE with other well-tested HFB solvers has been missing.

The new 2D HFB B-spline code HFB-AX developed in this work contains a number of new features aimed at speeding up the calculations, improving the accuracy, and optimizing the overall performance. First, we incorporated space inversion as a self-consistent symmetry. Since reflection-asymmetric ground-state deformations are present only in a handful of nuclei, this is not a serious limitation for studies of ground-state properties. Furthermore, we improved the iterative algorithm by means of the modified Broyden method. This resulted in significant convergence acceleration. We also made other optimizations to the HFB solver, which are described in the text. The performance and accuracy of HFB-AX has been carefully tested against other codes for different nuclear configurations. In short, we developed a fast coordinate-space 2D HFB solver that can be used to carry out large-scale calculations on leadership-class computers, while being also invaluable when providing test cases for the next generation of nuclear DFT tools.

This paper is organized as follows. Section II outlines the coordinate-space HFB approach in cylindrical coordinates and describes the numerical methods used. In Sec. III, numerical tests are presented, with an emphasis on comparison with other HFB solvers. The following examples are discussed: (i) study of the parity doublets in a two-center potential, in which the results of HFB-AX are compared with the multiresolution wavelet method and the HO expansion technique; (ii) comparison with the finite-difference 1D solver HFBRAD for spherical nuclei, both stable and neutron-rich; (iii) study of neutron-rich deformed ^{102,110}Zr and comparison with the axial 2D solvers HFBTHO and HFB-2D-LATTICE; and (iv) comparison with the axial 2D solver HFBTHO for strongly deformed configurations (i.e., the symmetric fission pathway in ^{240}Pu). Finally, Sec. IV contains the main conclusions of this paper.

II. THEORETICAL FRAMEWORK AND NUMERICAL METHOD

A. HFB equation in cylindrical coordinate space

The HFB equations in the coordinate-space representation can be written as [9,10,23]

$$\int d\mathbf{r}' \sum_{\sigma'} \begin{pmatrix} h(\mathbf{r}\sigma,\mathbf{r}'\sigma') - \lambda & \tilde{h}(\mathbf{r}\sigma,\mathbf{r}'\sigma') \\ \tilde{h}(\mathbf{r}\sigma,\mathbf{r}'\sigma') & -h(\mathbf{r}\sigma,\mathbf{r}'\sigma') + \lambda \end{pmatrix} \times \begin{pmatrix} \psi^{(1)}(\mathbf{r}'\sigma') \\ \psi^{(2)}(\mathbf{r}'\sigma') \end{pmatrix} = E \begin{pmatrix} \psi^{(1)}(\mathbf{r}\sigma) \\ \psi^{(2)}(\mathbf{r}\sigma) \end{pmatrix}, \tag{1}$$

where $(\mathbf{r},\sigma)$ are the particle spatial and spin coordinates, $h(\mathbf{r}\sigma,\mathbf{r}'\sigma')$ and $\tilde{h}(\mathbf{r}\sigma,\mathbf{r}'\sigma')$ are the particle-hole (p-h) and particle-particle (p-p) components of the single-quasiparticle Hamiltonian, respectively, $\psi_n^{(1)}(\mathbf{r}\sigma)$ and $\psi_n^{(2)}(\mathbf{r}\sigma)$ are the upper and lower components of the single-quasiparticle HFB wave function, and λ is the chemical potential. The spectrum of quasiparticle energies E is discrete for $|E| < -\lambda$ and continuous for $|E| > -\lambda$. By imposing that the eigenfunctions vanish at the edge of the box (box boundary conditions), the continuum is discretized. In practical calculations, the p-h channel is often modeled with the Skyrme energy density functional, while a zero-range δ pairing interaction is often used in the p-p channel. This choice is motivated by the fact that zero-range interactions yield the local HFB equations in coordinate space, which are easy to solve.

In the axially symmetric geometry, the third component of the single-particle angular momentum, Ω, is a good quantum number. The HFB wave function can thus be written as $\Psi_n(\mathbf{r},\Omega,q)$ where $\mathbf{r} = (\phi,\rho,z)$, $q = \pm\frac{1}{2}$ denotes the cylindrical isospin coordinates, and $\Omega = \pm\frac{1}{2}, \pm\frac{3}{2}, \pm\frac{5}{2}, \ldots$.

The corresponding HFB wave function can be written as [15]

$$\Psi_n(\mathbf{r},\Omega,q)=\begin{pmatrix}\psi^{(1)}_{n,\Omega,q}(\phi,\rho,z)\\ \psi^{(2)}_{n,\Omega,q}(\phi,\rho,z)\end{pmatrix}$$
$$=\frac{1}{\sqrt{2\pi}}\begin{pmatrix}e^{i(\Omega-\frac{1}{2})\phi}\psi^{(1)}_{n\Omega q}(\rho,z,\uparrow)\\ e^{i(\Omega+\frac{1}{2})\phi}\psi^{(1)}_{n\Omega q}(\rho,z,\downarrow)\\ e^{i(\Omega-\frac{1}{2})\phi}\psi^{(2)}_{n\Omega q}(\rho,z,\uparrow)\\ e^{i(\Omega+\frac{1}{2})\phi}\psi^{(2)}_{n\Omega q}(\rho,z,\downarrow)\end{pmatrix}. \quad (2)$$

Following the notation of Ref. [15], we introduce

$$U^{(1,2)}_{n\Omega q}(\rho,z)=\psi^{(1,2)}_{n\Omega q}(\rho,z,\uparrow),$$
$$D^{(1,2)}_{n\Omega q}(\rho,z)=\psi^{(1,2)}_{n\Omega q}(\rho,z,\downarrow), \quad (3)$$

where wave functions U and D denote the spin-up ($\sigma=\frac{1}{2}$) and spin-down ($\sigma=-\frac{1}{2}$) spinor components. Axial symmetry imposes time-reversal symmetry, and we need therefore only consider positive-Ω values. In terms of these wave functions, the particle density $\rho_q(\mathbf{r})$ and pairing density $\tilde{\rho}_q(\mathbf{r})$ can be written as

$$\rho_q(\mathbf{r})=\sum_\sigma\sum_{n\Omega}\psi^{(2)}_{n\Omega q}(\mathbf{r}\sigma)\psi^{(2)*}_{n\Omega q}(\mathbf{r}\sigma)$$
$$=\frac{1}{\pi}\sum_{\Omega=\frac{1}{2}}^{\Omega_{\max}}\sum_{E_n>0}^{E_{\max}}\left[\left|U^{(2)}_{n\Omega q}(\rho,z)\right|^2+\left|D^{(2)}_{n\Omega q}(\rho,z)\right|^2\right],$$
$$\tilde{\rho}_q(\mathbf{r})=-\sum_\sigma\sum_{n\Omega}\psi^{(2)}_{n\Omega q}(\mathbf{r}\sigma)\psi^{(1)*}_{n\Omega q}(\mathbf{r}\sigma) \quad (4)$$
$$=-\frac{1}{\pi}\sum_{\Omega=\frac{1}{2}}^{\Omega_{\max}}\sum_{E_n>0}^{E_{\max}}\left[U^{(2)}_{n\Omega q}(\rho,z)U^{(1)*}_{n\Omega q}(\rho,z)\right.$$
$$\left.+D^{(2)}_{n\Omega q}(\rho,z)D^{(1)*}_{n\Omega q}(\rho,z)\right].$$

In the above equations, the sums are limited by the quasiparticle energy cutoff $E_{\max}$, defining the effective range for a zero-range pairing force, and the angular momentum projection cutoff $\Omega_{\max}$. This way of truncating the continuum space is different from that in the spherical HFBRAD code [14], which employs a maximum $j_{\max}$ cutoff on the total single-particle angular momentum. This implies that even with the same energy cutoff, HFB-AX and HFBRAD have different pairing spaces. We shall return to this point later in Sec. III.

In the reflection-symmetric version of the code HFB-AX discussed in this paper, we assumed the space inversion as a self-consistent symmetry. Consequently, the quasiparticle wave functions are eigenstates of the parity operator $\hat{\mathcal{P}}$:

$$\hat{\mathcal{P}}\psi^{(1,2)}_{n,\Omega,q}(\phi,\rho,z)=\pi\,\psi^{(1,2)}_{n,\Omega,q}(\phi+\pi,\rho,-z), \quad (5)$$

i.e., parity $\pi=\pm$ is a good quantum number. The presence of conserved parity implies specific boundary conditions at $\rho=0$ and $z=0$ (see Table I). We also apply the box boundary conditions at the outer box boundaries; namely, the wave functions are put to zero at the edge of a 2D box $z_{\max}$ and $\rho_{\max}$. These boundary conditions are important for the construction of derivative operators.

TABLE I. Boundary conditions of HFB wave functions at $\rho=0$ and $z=0$ in HFB-AX. The single-particle states are labeled by Ω^π quantum numbers.

	$\rho=0$	$z=0$
$\Omega-\frac{1}{2}=$ even	$\frac{\partial U}{\partial\rho}\vert_{\rho=0}=0$	$\frac{\partial U}{\partial z}\vert_{z=0}=0$
$\pi=+1$	$D\vert_{\rho=0}=0$	$D\vert_{z=0}=0$
$\Omega-\frac{1}{2}=$ odd	$\frac{\partial D}{\partial\rho}\vert_{\rho=0}=0$	$\frac{\partial D}{\partial z}\vert_{z=0}=0$
$\pi=+1$	$U\vert_{\rho=0}=0$	$U\vert_{z=0}=0$
$\Omega-\frac{1}{2}=$ even	$\frac{\partial U}{\partial\rho}\vert_{\rho=0}=0$	$\frac{\partial D}{\partial z}\vert_{z=0}=0$
$\pi=-1$	$D\vert_{\rho=0}=0$	$U\vert_{z=0}=0$
$\Omega-\frac{1}{2}=$ odd	$\frac{\partial D}{\partial\rho}\vert_{\rho=0}=0$	$\frac{\partial U}{\partial z}\vert_{z=0}=0$
$\pi=-1$	$U\vert_{\rho=0}=0$	$D\vert_{z=0}=0$

In a given (Ω,q) block, the HFB Hamiltonian in Eq. (1) can be expressed through the mean fields h and $\tilde{h}$ with specified spin projections [15]:

$$\begin{pmatrix}h_{\uparrow\uparrow}-\lambda & h_{\uparrow\downarrow} & \tilde{h}_{\uparrow\uparrow} & \tilde{h}_{\uparrow\downarrow}\\ h_{\downarrow\uparrow} & h_{\downarrow\downarrow}-\lambda & \tilde{h}_{\downarrow\uparrow} & \tilde{h}_{\downarrow\downarrow}\\ \tilde{h}_{\uparrow\uparrow} & \tilde{h}_{\uparrow\downarrow} & -h_{\uparrow\uparrow}+\lambda & h_{\uparrow\downarrow}\\ \tilde{h}_{\downarrow\uparrow} & \tilde{h}_{\downarrow\downarrow} & h_{\downarrow\uparrow} & -h_{\downarrow\downarrow}+\lambda\end{pmatrix}. \quad (6)$$

The local Skyrme p-h Hamiltonian h has the usual form [9,10]

$$h_q(\mathbf{r},\sigma,\sigma')=-\nabla\cdot\frac{\hbar^2}{2m^*}\nabla+U_q-i\mathbf{B}_q\cdot(\nabla\times\boldsymbol{\sigma}), \quad (7)$$

where m^* is the effective mass, U_q is the central p-h mean-field potential including the Coulomb term for protons, and the spin-orbit potential with

$$\mathbf{B}_q=\tfrac{1}{2}W_q(\nabla\rho(\mathbf{r})+\nabla\rho_q(\mathbf{r})), \quad (8)$$

where W_q is the spin-orbit coupling strength.

The pairing Hamiltonian $\tilde{h}$ corresponding to the zero-range density-dependent δ interaction can be written as

$$\tilde{h}_q(\mathbf{r},\sigma,\sigma')=V_0^q\,\tilde{\rho}_q(\mathbf{r})F(\mathbf{r})\delta_{\sigma\sigma'}, \quad (9)$$

where $V_0^q<0$ is the pairing strength, and the pairing form factor $F(\mathbf{r})$ depends on the form of pairing Hamiltonian [24]:

$$F(\mathbf{r})=\begin{cases}1 & -\text{volume} \quad \text{pairing},\\ 1-\frac{\rho(\mathbf{r})}{\rho_0} & -\text{surface} \quad \text{pairing},\\ 1-\frac{\rho(\mathbf{r})}{2\rho_0} & -\text{mixed} \quad \text{pairing},\end{cases} \quad (10)$$

where $\rho_0=0.16$ fm^{-3}. The volume pairing interaction acts primarily inside the nuclear volume, while the surface pairing generates pairing fields peaked around or outside the nuclear surface. As discussed in Ref. [25], different forms of $F(\mathbf{r})$ can result in notable differences of pairing fields in diffused drip-line nuclei.

B. B-spline technique in HFB-AX

The lattice representation of wave functions and the HFB Hamiltonian used in this work closely follows that of the HFB-2D-LATTICE described in Ref. [17]. In HFB-AX, the wave

functions are discretized on a 2D grid (r_α, z_β) with the M-order B-splines:

$$\psi^{(1,2)}_{n\Omega^\pi q}(\rho_\alpha, z_\beta) = \sum_{i,j} B^M_i(\rho_\alpha) B^M_j(z_\beta) C^{ij(1,2)}_{n\Omega^\pi q}, \tag{11}$$

where C^{ij} is the matrix of expansion coefficients; $\alpha = 1, \ldots, N_\rho$, and $\beta = 1, \ldots, N_z$. The four components of the HFB wave functions (2) are thus represented in a matrix form. The derivative operators are constructed using the Galerkin method. In the B-spline representation, the HFB Hamiltonian acts on 2D wave functions like a tensorial operator, i.e.,

$$h^{\alpha\beta}_{\gamma\delta}\psi(\rho_\alpha, z_\beta) = \psi'(\rho_\gamma, z_\delta). \tag{12}$$

The HFB equation is solved by mapping the Hamiltonian tensor into a matrix, which is then diagonalized.

In the following, we give some details pertaining to Hamiltonian mapping, because the mapping rule is different with respect to the 16 individual blocks in Eq. (6). For the diagonal blocks, it is straightforward to map a tensor into a matrix (k, k'):

$$\begin{aligned}
h(\uparrow\uparrow)&: \begin{cases} k = (\beta-1)N_\rho + \alpha, \\ k' = (\delta-1)N_\rho + \gamma, \end{cases} \\
h(\downarrow\downarrow)&: \begin{cases} k = (\beta-1)N_\rho + \alpha + N_\rho N_z, \\ k' = (\delta-1)N_\rho + \gamma + N_\rho N_z, \end{cases} \\
-h(\uparrow\uparrow)&: \begin{cases} k = (\beta-1)N_\rho + \alpha + 2\times N_\rho N_z, \\ k' = (\delta-1)N_\rho + \gamma + 2\times N_\rho N_z, \end{cases} \\
-h(\downarrow\downarrow)&: \begin{cases} k = (\beta-1)N_\rho + \alpha + 3\times N_\rho N_z, \\ k' = (\delta-1)N_\rho + \gamma + 3\times N_\rho N_z. \end{cases}
\end{aligned} \tag{13}$$

Following the same rule, the bra and ket vectors are mapped into vectors with indexes k and k', respectively. It is more complicated to map the off-diagonal blocks of Eq. (6). For the four ket vectors, the mapped index k should correspond to different columns of the Hamiltonian blocks. For example, the index of the first ket component $U^{(1)}$ should correspond to the upper index of the first column of Eq. (6):

$$\begin{pmatrix} U^{(1)*} & D^{(1)*} & U^{(2)*} & D^{(2)*} \end{pmatrix} \begin{pmatrix} \overline{h^{\alpha\beta}(\uparrow\uparrow) - \lambda} & h(\uparrow\downarrow) & \tilde{h}(\uparrow\uparrow) & \tilde{h}(\uparrow\downarrow) \\ h^{\alpha\beta}(\downarrow\uparrow) & h(\downarrow\downarrow) - \lambda & \tilde{h}(\downarrow\uparrow) & \tilde{h}(\downarrow\downarrow) \\ \tilde{h}^{\alpha\beta}(\uparrow\uparrow) & \tilde{h}(\uparrow\downarrow) & -h(\uparrow\uparrow) + \lambda & -h(\uparrow\downarrow) \\ \underline{\tilde{h}^{\alpha\beta}(\downarrow\uparrow)} & \tilde{h}(\downarrow\downarrow) & -h(\downarrow\uparrow) & -h(\downarrow\downarrow) + \lambda \end{pmatrix} \times \begin{pmatrix} \overline{U^{(1)}(\rho_\alpha z_\beta)} \\ D^{(1)} \\ U^{(2)} \\ D^{(2)} \end{pmatrix}. \tag{14}$$

For the four bra vectors, the mapped index k' corresponds to different rows of the Hamiltonian. For example, the index of the first bra component $U^{(1)*}$ corresponds to the lower index of the first row of Eq. (6):

$$\begin{pmatrix} \overline{|U^{(1)*}(\rho_\gamma z_\delta)|} & D^{(1)*} & U^{(2)*} & D^{(2)*} \end{pmatrix} \begin{pmatrix} \overline{h_{\gamma\delta}(\uparrow\uparrow) - \lambda} & h_{\gamma\delta}(\uparrow\downarrow) & \tilde{h}_{\gamma\delta}(\uparrow\downarrow) & \tilde{h}_{\gamma\delta}(\downarrow\downarrow) \\ h(\downarrow\uparrow) & h(\downarrow\downarrow) - \lambda & \tilde{h}(\downarrow\uparrow) & \tilde{h}(\downarrow\downarrow) \\ \tilde{h}(\uparrow\uparrow) & \tilde{h}(\uparrow\downarrow) & -h(\uparrow\uparrow) + \lambda & -h(\uparrow\downarrow) \\ \tilde{h}(\downarrow\uparrow) & \tilde{h}(\downarrow\downarrow) & -h(\downarrow\uparrow) & -h(\downarrow\downarrow) + \lambda \end{pmatrix} \begin{pmatrix} U^{(1)} \\ D^{(1)} \\ U^{(2)} \\ D^{(2)} \end{pmatrix}. \tag{15}$$

In this way, the HFB Hamiltonian is mapped into a matrix of the rank $4 \times N_\rho N_z$. The resulting HFB Hamiltonian matrix is diagonalized using LAPACK routines [26].

The Coulomb potential is obtained by directly integrating the Poisson equation,

$$\nabla^2\phi(\rho, z) = -4\pi e^2 \rho_p(\rho, z), \tag{16}$$

where ϕ is the Coulomb potential and ρ_p is the proton density. The Poisson equation, discretized on a B-spline grid, can be written in a matrix form. The boundary conditions at large distances are given by the multipole expansion of the Coulomb potential as in Ref. [17]. The gradient of the Coulomb potential at $z = 0$ or $\rho = 0$ is set to be zero because of the symmetries imposed. These boundary conditions are incorporated in the lattice representation of the Laplace operator.

C. Performance improvements in HFB-AX

The size of the HFB Hamiltonian matrix depends on the box sizes $z_{\max}$ and $\rho_{\max}$, the largest distance between neighboring mesh points in the grid h (the B-spline grid is not uniform), and the order of B-splines M. Consequently, for large and refined grids, the diagonalization time becomes a bottleneck. For example, for ^{120}Sn with a box of $R = z_{\max} = \rho_{\max} = 19.2$ fm, a maximum grid size of $h = 0.6$ fm, and $M = 13$, the Hamiltonian matrix is about 0.45 GB of storage, and one diagonalization takes about 30 CPU minutes.

However, since the diagonalization of HFB matrices corresponding to different Ω^π blocks can be done independently in different processors, this part of HFB-AX can be parallelized using the standard Message Passing Interface library [27].

For ^{120}Sn with $\Omega_{\max} = 33/2$ cutoff, about 70 processors are utilized. The precision of the derivative operators is crucial for the precision of the HFB eigenstates. By distributing the diagonalization over many processors, one can perform calculations with larger boxes, denser grids, and higher order B-splines. In addition, by taking advantage of the reflection symmetry, N_z can be reduced; hence the rank of the Hamiltonian matrix is scaled down by a factor of slightly less than 2. Consequently, the diagonalization process, which takes most of the execution time, can be speeded up by a factor greater than 8.

For the diagonalization, we employ the LAPACK DGEEV routine [26]. This routine diagonalizes a nonsymmetric matrix using a QR algorithm [28]. However, due to energy cutoff induced by the use of zero-range pairing interaction, it is not necessary to compute all eigenvectors. For this reason, we modified DGEEV so that it yields eigenvectors only within the required energy window. In this way, the diagonalization time for ^{120}Sn is further reduced by one-third.

To optimize the convergence of HFB iterations, we take the HF-BCS densities to warm-start the self-consistent process. Furthermore, we have implemented the so-called modified Broyden mixing [29] to accelerate the convergence rate. The modified Broyden method is a quasi-Newton algorithm used to solve large sets of self-consistent nonlinear equations. In substance, it relies on estimating the difference at the m-th iteration:

$$\boldsymbol{F}^{(m)} = \boldsymbol{V}_{\text{out}}^{(m)} - \boldsymbol{V}_{\text{in}}^{(m)}, \tag{17}$$

where $\boldsymbol{V}$ is an N-dimensional vector containing the unknowns characteristic of the problem. The self-consistency condition requires that the solution $\boldsymbol{V}^*$ be a fixed point of the iteration: $\boldsymbol{I}(\boldsymbol{V}^*) = \boldsymbol{V}^*$. For the commonly used linear mixing, the input at iteration $m+1$ is given as

$$\boldsymbol{V}_{\text{in}}^{(m+1)} = \boldsymbol{V}_{\text{in}}^{(m)} + \alpha \boldsymbol{F}^{(m)}, \tag{18}$$

where α is a constant between 0 and 1. In contrast, to estimate the next step, the modified Broyden mixing utilizes information obtained in the previous M_B iterations. Recent implementations of this technique to the HFB problem have demonstrated that convergence can generally be obtained within 20–30 iterations [30]. In HFB-AX, the vector $\boldsymbol{V}$ consists of local densities and their derivatives at lattice mesh points:

$$\boldsymbol{V} \equiv \{\rho_q, \tau_q, \nabla \cdot \mathbf{J}_q, \tilde{\rho}_q, \nabla^2 \rho_q, \nabla_\rho \rho_q, \nabla_z \rho_q\}. \tag{19}$$

The dimension of $\boldsymbol{V}$ is thus $14 \times N_\rho \times N_z$.

To demonstrate the performance of the method, we consider ^{22}O in a 2D square box of $R = 12$ fm, $h = 0.6$ fm and $M = 11$. The calculations were carried out at ORNL on a Cray XT3 supercomputer having 2.6 GHz processors. Without reflection symmetry, one diagonalization takes about 15 min of CPU time. With reflection symmetry imposed, one diagonalization needs about 100 s with the modified DGEEV. The calculations with Broyden mixing with $M_B = 7$ are displayed in Fig. 1. The actual variation of the binding energy is within 0.1 keV after 30 iterations. This is to be compared with linear mixing with $\alpha = 0.6$, which requires over 80 iterations to reach similar convergence. Both calculations show precision limitations due to the numerical noise inherent to the mesh assumed. As in the examples discussed in Ref. [30], the Broyden method, as implemented in HFB-AX, provides impressive performance gains. The numerical speedup is particularly helpful for heavy nuclei and for constrained calculations, which usually require many self-consistent iterations.

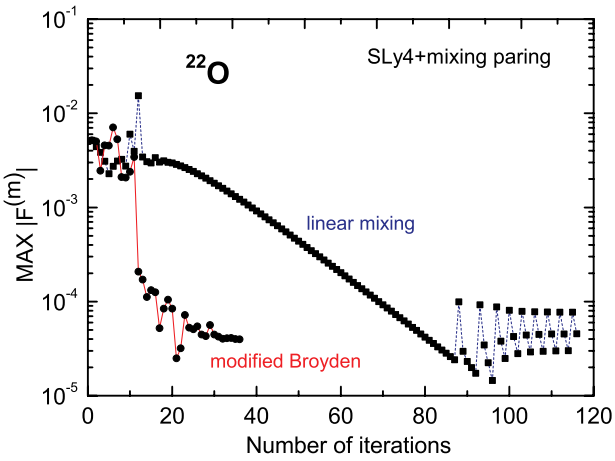

FIG. 1. (Color online) Comparison between linear mixing (squares) and modified Broyden method (circles) in HFB-AX for ^{22}O. The largest element of $|\boldsymbol{F}^{(m)}|$ is shown as a function of the number of iterations m. See text for details.

III. BENCHMARKING OF HFB-AX AND TYPICAL APPLICATIONS

This section discusses HFB-AX test cases. First, the absolute accuracy of the one-body HF solver is tested using the adaptive multiresolution method and a simple two-center potential. A comparison with a HO expansion method is carried out also for the HFB solver with a schematic pairing potential. Thereafter follows a series of realistic calculations in which HFB-AX is compared with the spherical coordinate-space code HFBRAD and the axial code HFBTHO. In all these realistic tests, the Skyrme functional SLy4 [31] was used in the p-h channel, augmented by different density-dependent δ functionals [Eq. (9)] in the p-p channel.

A. Two-center potential: Comparison with HO and wavelet expansions

The accuracy of the HFB-AX calculations in the p-h channel has been tested using an adaptive multiwavelet basis. To this end, we employed the MADNESS framework [21]. The details regarding our particular realization of the wavelet basis expansion can be found in Refs. [22,32].

As a test case, we choose an axial two-center inverted-cosh potential:

$$V(\rho, z) = V_0 \left[f(\rho, z+\zeta) + f(\rho, z-\zeta) \right], \tag{20}$$

where the inverted-cosh form factor is

$$f(\rho, z) = \frac{1}{1 + e^{-R_0/a} \cosh(\sqrt{\rho^2 + z^2}/a)}, \tag{21}$$

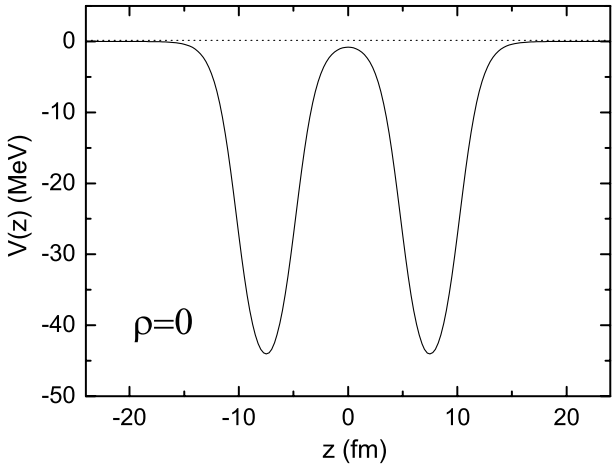

FIG. 2. Two-center inverted-cosh potential of Eq. (20) as a function of z at $\rho = 0$. The two centers are 15 fm apart ($\zeta = 7.5$ fm) and $V_0 = -50$ MeV, $R_0 = 2$ fm, and $a = 1$ fm.

and V_0, R_0, and a are the potential's depth, radius, and diffuseness, respectively, and 2ζ is the distance between the two centers. A cross section of the potential used in our test calculations is shown in Fig. 2 along the z axis at $\rho = 0$. The two centers are well separated; hence, the ability to predict a small parity splitting between the eigenstate doublets provides a stringent test for the B-spline Schrödinger equation solver of HFB-AX.

In addition to the mean-field potential (20), we also considered the spin-orbit term in the usual Thomas form:

$$V_{\mathrm{SO}}(\rho, z) = -i\lambda_0 \left(\frac{\hbar}{2mc}\right)^2 \nabla V(\rho, z) \cdot (\boldsymbol{\sigma} \times \boldsymbol{\nabla}), \quad (22)$$

where $\lambda_0 = 5.0$, and the numerical values of fundamental constants were taken as $\hbar^2/2m = 20.721246$ fm^2, $\hbar c = 197.32696$ MeV fm, and $mc^2 = 939.56535$ MeV. The corresponding one-body Schrödinger equation reads

$$\left[-\frac{\hbar^2}{2m}\nabla^2 + V(\rho, z) + V_{SO}(\rho, z)\right]\varphi(\rho, z, \phi) = E\varphi(\rho, z, \phi), \quad (23)$$

where $\varphi(\rho, z, \phi)$ is a two-component spinor wave function. Physically, the spin-orbit potential is necessary to model a realistic nuclear potential. Mathematically, it involves differential operators and therefore tests the accuracy of the techniques employed.

Table II displays the lowest eigenvalues of the two-center potential (20) obtained in three expansion methods. In the HO expansion calculation, we took $N_{\mathrm{sh}} = 20$ and 30 shells of the spherical oscillator with $\hbar\omega_0 = 5.125$ MeV (as it turned out, the use of a stretched basis was not particularly advantageous). The size of the $\Omega^\pi = \frac{1}{2}^+$ Hamiltonian block is 121 and 256 for $N_{\mathrm{sh}} = 20$ and 30, respectively; i.e., the matrix size is more than doubled in the latter case. In the HFB-AX calculation with $M = 13$, we used a square box of $R = 25.2$ fm and $h = 0.6$ fm. (The values of $N_{\mathrm{sh}} = 20$ in HO and $h = 0.6$ fm in HFB-AX are typical for realistic Skyrme-HFB calculations.) In the wavelet variant [22,32], the absolute accuracy was assumed to be 10^{-5}.

It is seen that the accuracy of B-spline expansion is excellent, both for the absolute energies and for the parity splitting. The HO basis with $N_{\mathrm{sh}} = 20$ performs rather poorly, especially for parity splitting and for the energies of the highest (halo) states. That is to be expected, of course, for a two-center potential expanded in a one-center basis. It is only at $N_{\mathrm{sh}} = 30$, not practical in large-scale DFT calculations, that a good agreement with wavelets and HFB-AX is obtained. In all variants, there is a perfect degeneracy of $p_{3/2}$ doublets with $\Omega = \frac{1}{2}$ and $\Omega = \frac{3}{2}$.

The results with the inclusion of the spin-orbit term, which lifts the degeneracy between $\Omega = \frac{1}{2}$ and $\frac{3}{2}$ levels, are given in Table III. It is seen that the general excellent agreement between B-spline and wavelet variants holds, and that HO with $N_{\mathrm{sh}} = 20$ performs rather poorly, especially for the halo state.

Finally, the single-particle spectrum of a two-center potential is illustrated in Fig. 3 as a function of the intercenter distance. A transition to a dimer-like spectrum is clearly seen at distances greater than 6 fm. Our tests nicely illustrate the ability of the B-spline technique (thus, HFB-AX) to handle a two-center problem encountered, e.g., in fission or fusion [33].

To provide benchmark results when pairing is included, we solved the HFB equations with the two-center potential as in Eq. (23) in the particle-hole channel and the schematic pairing

TABLE II. Ten lowest eigenvalues of the two-center potential (20) obtained using the HO, B-spline, and wavelet expansions. All energies are in MeV. For more details, see text.

State No.	Ω^π	HO $N_{\mathrm{sh}} = 20$	HO $N_{\mathrm{sh}} = 30$	B-spline $h = 0.6$	Wavelets
1	$1/2^+$	−22.23916	−22.24008	−22.24011	−22.24011
2	$1/2^-$	−22.23816	−22.23995	−22.23998	−22.23998
3	$1/2^+$	−9.21514	−9.22047	−9.22050	−9.22050
4	$3/2^-$	−9.20359	−9.21256	−9.21260	−9.21260
5	$1/2^-$	−9.20359	−9.21256	−9.21260	−9.21260
6	$3/2^+$	−9.20589	−9.21126	−9.21129	−9.21129
7	$1/2^+$	−9.20589	−9.21126	−9.21129	−9.21129
8	$1/2^-$	−9.19743	−9.20590	−9.20595	−9.20595
9	$1/2^+$	−1.70724	−1.72402	−1.72503	−1.72514
10	$1/2^-$	−1.49218	−1.52486	−1.52672	−1.52690

TABLE III. Similar to Table II, except for the two-center double-cosh potential with the spin-orbit term.

State No.	Ω^π	HO $N_{\rm sh} = 20$	HO $N_{\rm sh} = 30$	B-spline $h = 0.6$	Wavelets
1	$1/2^+$	−22.23916	−22.24008	−22.24011	−22.24011
2	$1/2^-$	−22.23816	−22.23995	−22.23998	−22.23998
3	$1/2^+$	−9.43145	−9.43659	−9.43663	−9.43662
4	$3/2^-$	−9.42314	−9.43199	−9.43203	−9.43202
5	$3/2^+$	−9.42561	−9.43078	−9.43081	−9.43080
6	$1/2^-$	−9.41931	−9.42783	−9.42788	−9.42788
7	$1/2^+$	−8.77250	−8.77825	−8.77828	−8.77828
8	$1/2^-$	−8.76475	−8.77380	−8.77384	−8.77383
9	$1/2^+$	−1.70727	−1.72405	−1.72506	−1.72516
10	$1/2^-$	−1.49222	−1.52490	−1.52675	−1.52693

potential:

$$\tilde{h}(\mathbf{r}) = 0.05 \times V(\rho, z), \tag{24}$$

with $V(\rho, z)$ given by Eq. (20). For the chemical potential, we assumed a fixed value of $\lambda = -5$ MeV. Although the HFB wavelet solver is still under development, it is instructive to compare B-spline and HO results. The energies E_i and occupation numbers v_i^2 of the eight bound states ($E_i < -\lambda$) of the simple HFB Hamiltonian are shown in Table IV. One can see that the HO expansion method with $N_{\rm sh} = 25$ yields HFB eigenvalues that are reasonably close to those with B-spline.

B. Spherical limit: Comparison with HFBRAD and HFBTHO

The performance of HFB-AX at the spherical limit can be assessed by comparing it against the accurate 1D radial coordinate code HFBRAD, based on the direct integration of the system of coupled radial differential equations [9,14]. The tests have been carried out for the nucleus ^{120}Sn, which is often used for comparing HFB solvers [8,17] in the limit of spherical shape and nonzero neutron pairing.

The precision of HFB calculations in coordinate space is primarily determined by the size of the mesh used. We calculated ^{120}Sn with the fixed-box size ($R = 19.2$ fm) but with different mesh steps and B-spline orders. In our calculations, we took the volume δ pairing interaction with the pairing strength $V_0 = -187.05$ MeV fm^3 adjusted to the average experimental neutron pairing gap $\Delta_n = 1.245$ MeV. For the pairing configuration space, we adopted the commonly used equivalent energy cutoff of 60 MeV [8]. As both codes are written in different geometries, the quasiparticle continuum is discretized differently in HFBRAD and HFB-AX. In HFBRAD, all partial waves with $j \leqslant j_{\rm max} = 33/2$ were considered, while in HFB-AX we imposed a cutoff on j_z: $\Omega_{\rm max} = 33/2$. For the sake of comparison, the pairing regularization option in HFBRAD has been turned off. Also, we adopted the same values of the fundamental constants as in Ref. [8]: $\hbar^2/2m = 20.73553$ MeV and $e^2 = 1.439978$ MeV fm.

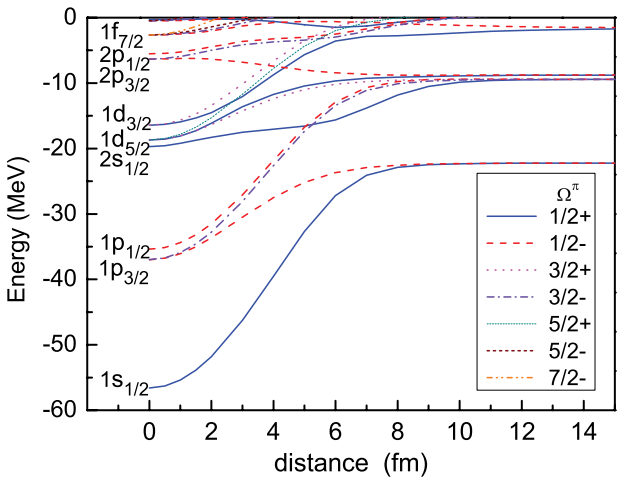

FIG. 3. (Color online) Eigenvalues of a two-center inverted-cosh potential with the spin-orbit term calculated in HFB-AX as functions of the distance between two centers 2ζ.

Table V displays various contributions to the binding energy $E_{\rm tot}$ of ^{120}Sn, i.e., kinetic energy $E_{\rm kin}$ for protons and neutrons, Coulomb energy E_C, neutron pairing energy $E^n_{\rm pair}$, neutron pairing gap Δ_n, and Fermi level λ_n, and the sum

$$\tilde{E}_{\rm kin} = E_{\rm kin} + E_{\rm pair} \tag{25}$$

for neutrons. As discussed in Refs. [34–36], while for zero-range pairing the individual values of $E_{\rm kin}$ and $E_{\rm pair}$ are divergent with respect to the cutoff energy of the pairing window, their sum [Eq. (25)] is less sensitive to the cutoff

TABLE IV. Eight quasiparticle energies ($E_i < -\lambda$) of a schematic two-center HFB Hamiltonian obtained using the HO expansion method with $N_{\rm sh} = 25$ and the B-spline method using the same mesh as in Tables II and III. All energies are in MeV. See text for details.

State No.	Ω^π	HO E_i	B-spline E_i	HO v_i^2	B-spline v_i^2
1	$1/2^+$	4.58515	4.53410	0.98377	0.96998
2	$1/2^-$	4.58131	4.53438	0.98371	0.96478
3	$3/2^+$	4.57997	4.53429	0.98369	0.96939
4	$3/2^-$	4.57769	4.53155	0.98363	0.96430
5	$1/2^-$	3.94644	3.90778	0.97854	0.96848
6	$1/2^+$	3.94287	3.90552	0.97845	0.96845
7	$1/2^+$	3.52045	3.52222	0.00579	0.00853
8	$1/2^-$	3.31861	3.32172	0.00600	0.00789

TABLE V. Results of spherical HFB + SLy4 calculations with volume pairing for ^{120}Sn using HFB-AX with different mesh size h and B-spline order M. The results of the precision radial code HFBRAD are shown for comparison. The static proton pairing is zero. All energies are in MeV; h is in fm.

E	$h = 0.64$ $M = 11$	$h = 0.6$ $M = 11$	$h = 0.6$ $M = 13$	$h = 0.15$ HFBRAD
$E_{\rm tot}$	−1018.304	−1018.271	−1018.356	−1018.362
E_C	347.636	347.642	347.577	347.558
$E^p_{\rm kin}$	831.520	831.512	831.534	831.520
$E^n_{\rm kin}$	1339.516	1339.553	1339.562	1339.598
$E^n_{\rm pair}$	−10.253	−10.253	−10.253	−10.278
$\tilde{E}^n_{\rm kin}$	1329.263	1329.300	1329.309	1329.320
Δ_n	1.2451	1.2451	1.2451	1.2450
λ_n	−7.9950	−7.9950	−7.9950	−7.9953

energy and to actual treatment of the discretized quasiparticle continuum. The general agreement between HFB-AX and HFBRAD is excellent, in particular in the $h = 0.6$ fm, $M = 13$ variant, with most quantities agreeing within 10 keV. As expected, the largest difference is seen for $E^n_{\rm kin}$ and $E^n_{\rm pair}$ because of the slightly different treatment of the unbound spectrum in the two models; however, the sum $\tilde{E}_{\rm kin}$ is well reproduced by HFB-AX.

The HFB results with mixed pairing obtained in HFB-AX, HFBRAD, and HFBTHO are shown in Table VI.

The pairing strength in HFB-AX was taken as $V_0 = -284.29$ MeV fm^3, as compared to −284.36 and −284.10 MeV fm^3 in HFBRAD and HFBTHO, respectively [8]. In HFBTHO calculations, 25 shells of the transformed HO basis were used. Again, the agreement between HFB-AX and HFBRAD is excellent, and the total binding energies obtained in the three methods agree within 12 keV. As expected, the largest differences are seen for $E_{\rm kin}$. In particular, HFBTHO underestimates the neutron (proton) kinetic energy by about 200 (100) keV. This deviation is partly due to different representations of the kinetic energy operator in the coordinate space and in the transformed oscillator basis, and partly due to the different continuum space (see the discussion above).

TABLE VI. Similar to Table V, except for the mixed pairing interaction. HFB-AX results are compared with those of HFBRAD and HFBTHO of Ref. [8].

E	$h = 0.6$ $M = 13$	$h = 0.1$ HFBRAD	HFBTHO
$E_{\rm tot}$	−1018.795	−1018.791	−1018.777
E_C	347.442	347.400	347.370
$E^p_{\rm kin}$	830.856	830.848	830.735
$E^n_{\rm kin}$	1340.675	1340.668	1340.458
$E^n_{\rm pair}$	−12.491	−12.467	−12.467
$\tilde{E}^n_{\rm kin}$	1328.184	1328.201	1327.991
Δ_n	1.2448	1.2446	1.2447
λ_n	−8.0186	−8.0181	−8.0168

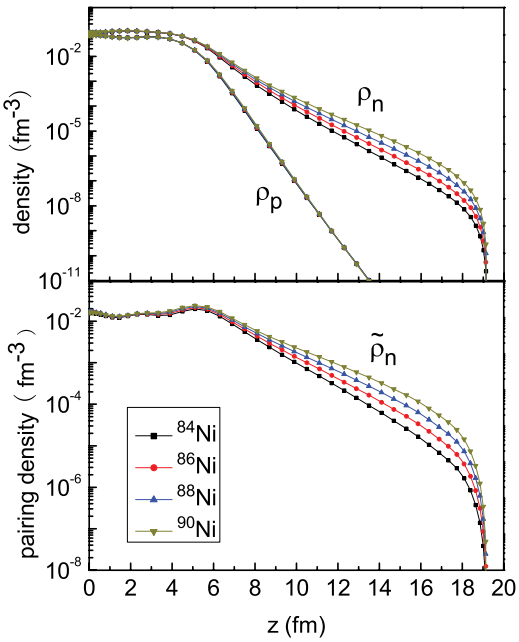

FIG. 4. (Color online) Proton (top) and neutron pairing (bottom) densities calculated in HFB-AX for ^{84,86,88,90}Ni. Proton pairing is zero.

C. Weak binding regime: Comparison with HFBRAD

Neutron-rich nuclei are unique laboratories of neutron pairing. In weakly bound nuclei, pairing fields are affected by the coupling to the continuum space, and this coupling can significantly modify pair distributions [10,25,37,38]. In Sec. III B we demonstrated that HFB-AX performs very well for a stable spherical nucleus ^{120}Sn. To evaluate the performance of HFB-AX for spherical neutron-rich nuclei, we discuss in this section the ground-state properties of even-even ^{84,86,88,90}Ni isotopes, which are expected to be weakly bound [12,39–41].

In our test calculations, we adopted the surface pairing with the strength adjusted to ^{120}Sn ($V_0 = -512.6$ MeV fm^3). Results of HFBRAD and HFB-AX calculations are listed in Table VII. The nucleus ^{90}Ni is a drip-line system, and its stability is strongly influenced by the particular form of the pairing interaction. Indeed, it is only bound with surface pairing. When volume and mixed pairing interactions are employed, ^{90}Ni is predicted to have a positive neutron chemical potential (see Ref. [25] for more discussion concerning this point).

The local particle and pairing densities of drip-line even-even Ni isotopes are shown in Fig. 4. A gradual increase of the neutron skin when approaching ^{90}Ni is clearly visible. The proton density, on the other hand, is only weakly affected by the outermost neutrons.

The systematic comparison between HFB-AX and HFBRAD is given in Table VII. For the binding energy, the agreement is very good, including the border-line system ^{90}Ni. The neutron pairing energy increases as one approaches the neutron drip line. This is consistent with the systematic behavior of pairing densities shown in Fig. 4.

For ^{84}Ni, HFB-AX and HFBRAD yield similar pairing properties and kinetic energies. However, with increasing neutron number, the difference between the values of $\tilde{E}^n_{\rm kin}$ obtained in

TABLE VII. Comparison between HFB-AX and HFBRAD with SLy4 p-h functional and surface pairing for drip-line nuclei ^{84,86,88,90}Ni. The same box $R = 19.2$ fm is used in both cases. The angular momentum cutoff was taken at $j_{\max} = 33/2$ in HFBRAD and $\Omega_{\max} = 33/2$ in HFB-AX. All energies are in MeV.

E	^{84}Ni		^{86}Ni		^{88}Ni		^{90}Ni	
	HFBRAD	HFB-AX	HFBRAD	HFB-AX	HFBRAD	HFB-AX	HFBRAD	HFB-AX
$E_{\rm tot}$	−654.919	−654.899	−656.915	−656.955	−658.215	−658.193	−658.877	−658.856
E_C	122.797	122.806	122.215	122.228	121.621	121.640	121.018	121.056
$E^p_{\rm kin}$	430.468	430.460	426.311	426.330	422.152	422.206	418.027	418.204
$E^n_{\rm kin}$	1084.511	1084.577	1116.835	1116.782	1148.387	1148.179	1179.697	1178.956
$E^n_{\rm pair}$	−30.892	−30.890	−36.733	−37.080	−43.179	−43.727	−49.926	−50.807
$\tilde{E}^n_{\rm kin}$	1053.619	1053.687	1080.102	1079.702	1105.208	1104.452	1129.771	1128.149
Δ_n	1.485	1.486	1.613	1.617	1.742	1.746	1.862	1.864
λ_n	−1.455	−1.454	−1.062	−1.068	−0.709	−0.718	−0.399	−0.417

the two models gradually grows, reaching over 1.6 MeV in ^{90}Ni. At the same time, the difference between $E^p_{\rm kin}$ values is smaller by an order of magnitude. This systematic difference between HFB-AX and HFBRAD when approaching the neutron drip line can be traced back to different angular momentum truncations, i.e., to the pairing configuration space structure. In HFBRAD, the s.p. angular momentum cutoff is $j_{\max} = 33/2$, while in the HFB-AX, the cutoff is done in terms of the s.p. angular momentum projection, i.e., $\Omega_{\max} = 33/2$. Consequently, in HFB-AX contributions from high-j, low-Ω continuum states, absent in HFBRAD, are present. In Sec. III B, we showed that for the well-bound nucleus ^{120}Sn, this difference in the continuum phase space is insignificant. However, for nuclei close to the drip line, where the contribution from unbound states is far more important, the situation is very different.

To quantify this point, we performed calculations for ^{90}Ni with $j_{\max} = 49/2$ in HFBRAD and $\Omega_{\max} = 49/2$ in HFB-AX. The results are displayed in Table VIII. The variations in the proton kinetic energy between various variants of calculations are small, suggesting that the kinetic energy operator is well represented by both HFBRAD and HFB-AX with the grids assumed. Also, the binding energy changes little, ∼30 keV, when the j or Ω cutoff is increased. In the larger j window, $\tilde{E}^n_{\rm kin}$ in HFBRAD is reduced by about 1 MeV; the corresponding change in HFB-AX is much smaller, ∼200 keV. This result indicates that the high-j continuum contributions play an important role in the structure of ^{90}Ni. A need for an appreciable angular momentum cutoff in the description of weakly bound nuclei, especially for surface-like pairing interactions, has been pointed out in Ref. [42].

TABLE VIII. Similar to Table VII, except for ^{90}Ni with the angular momentum cutoff $j_{\max} = 49/2$ in HFBRAD and $\Omega_{\max} = 49/2$ in HFB-AX. All energies are in MeV.

	HFBRAD	HFB-AX
$E_{\rm tot}$	−658.911	−658.881
E_C	121.038	121.060
$E^p_{\rm kin}$	418.165	418.233
$E^n_{\rm kin}$	1179.073	1178.843
$E^n_{\rm pair}$	−50.326	−50.892
$\tilde{E}^n_{\rm kin}$	1128.747	1127.951
Δ_n	1.860	1.864
λ_n	−0.410	−0.420

D. Deformed, weakly bound case: Comparison with HFBTHO

One of the objectives of HFB-AX is to precisely solve the HFB equations for axially deformed nuclei, in particular at very large deformations and/or at the limit of weak binding. In this context, the neutron-rich Zr isotopes with $A \sim 110$ are very useful testing grounds, as they are known to have very large prolate deformations [17]. In this section, we compare axial HFB-AX and HFBTHO calculations for the nuclei ^{102,110}Zr, which exhibit deformed neutron skin.

Table IX shows the results of deformed calculations for ^{102}Zr and ^{110}Zr with the same parameters as in spherical calculations for ^{120}Sn displayed in Table VI. In HFBTHO, deformed wave functions were expanded in the space of 20 stretched HO shells. The binding energies in HFB-AX are greater by about 110–140 keV than those of HFBTHO. This is understandable as HFBTHO with 20 shells also underestimates the binding energy of ^{120}Sn by about 150 keV [8]. In Table IX

TABLE IX. Results of deformed HFB-AX and HFBTHO HFB + SLy4 calculations for ^{102}Zr and ^{110}Zr with mixed pairing. All energies are in MeV. The quadrupole moments are in fm^2.

	^{102}Zr		^{110}Zr	
	HFB-AX	HFBTHO	HFB-AX	HFBTHO
$E_{\rm tot}$	−859.649	−859.540	−893.983	−893.840
E_C	231.149	231.084	226.758	226.712
$E^p_{\rm kin}$	651.309	651.099	632.115	631.882
$E^n_{\rm kin}$	1202.050	1201.990	1368.206	1368.201
$E^n_{\rm pair}$	−3.261	−3.535	−3.200	−3.323
$\tilde{E}^n_{\rm kin}$	1198.789	1198.455	1365.006	1364.878
Δ_n	0.672	0.700	0.636	0.652
λ_n	−5.431	−5.435	−3.552	−3.543
Q^p_{20}	410.08	411.31	444.02	443.90
Q^n_{20}	638.19	639.41	788.32	786.63

TABLE X. Comparison between HFB-2D-LATTICE (second column) and HFB-AX (third column) for ^{102}Zr. Calculation parameters are the same as in Ref. [15], i.e., $V_0 = -170$ MeV fm^3, $\Omega_{\max} = 11/2$, $R = 12$ fm, and $N_p = N_z = 19$. The results of HFB-AX with the same density functional but the standard box $R = 19.2$ fm and larger pairing cutoff $\Omega_{\max} = 33/2$ are displayed in the last column (HFB-AX′). All energies are in MeV. The mass rms radius $R_{\rm rms}$ is in fm.

	HFB-2D-LATTICE	HFB-AX	HFB-AX′
$E_{\rm tot}$	−859.61	−859.19	−859.25
λ_n	−5.46	−5.47	−5.45
λ_p	−12.10	−12.05	−12.06
Δ_n	0.31	0.28	0.43
Δ_p	0.34	0.37	0.40
$R_{\rm rms}$	4.58	4.58	4.58
β_2	0.431	0.434	0.43

we only show neutron pairing (proton pairing correlations in ^{110}Zr vanish due to a deformed proton subclosure at $Z = 40$). It is gratifying to see that the energies and quadrupole moments of ^{102}Zr and ^{110}Zr are very close in HFB-AX and HFBTHO, in spite of the fairly different computational strategies implemented in these two codes.

To compare HFB-AX with the Vanderbilt lattice code HFB-2D-LATTICE, we calculated the deformed nucleus ^{102}Zr assuming the same parameters as in Ref. [15], i.e., a fairly small box radius $R = 12$ fm, coarse grid, and very low cutoff $\Omega_{\max} = 11/2$. The ground state of ^{102}Zr is reflection-symmetric; thus, apart from the fact that the box of HFB-2D-LATTICE is twice as large as that of HFB-AX, the codes are supposed to produce the same result. As seen in Table X, this is almost the case: the difference for the binding energy is around 400 keV. We believe that this could be attributed to a slightly different structure of the discretized positive-energy continuum in the two codes. Indeed, the average pairing gaps predicted in the two codes are ∼30 keV apart. To confirm this, we performed another calculation for ^{102}Zr in a larger space, i.e., $R = 19.2$ fm, $h = 0.6$ fm, and $\Omega_{\max} = 33/2$. While the total energy is only weakly affected, there is an appreciable increase in the pairing gaps. This result, together with the discussion of ^{90}Ni in Sec. III C, underlines the importance of using large boxes and sizable pairing spaces for the description of neutron-rich systems.

The results displayed in Table X can also be compared with the predictions of the 2D finite-difference approach in Ref. [18] (cf. Table I therein). The latter method yields the binding energy of ^{102}Zr, which is about 3 MeV above the HFB-AX and HFB-2D-LATTICE values. As discussed in Ref. [18], this is probably due to the use of the finite-difference approximation for the differential operators, which is much less accurate than the B-spline representation.

Proton and neutron density distributions in ^{110}Zr are displayed in Fig. 5 (in two dimensions, to better show the deformed shape) and Fig. 6 (in logarithmic scale, to better show the asymptotic behavior). The appearance of the neutron skin beyond the nuclear surface is clearly seen. The density contours in Fig. 5 can be compared with the result of the HFB-2D-LATTICE shown in Fig. 6 of Ref. [17], and there seems to be a good agreement between the two sets of calculations. In particular, the small depression of the density in the nuclear interior, due to shell effects, is present in both cases. Another interesting feature is the rather constant value of the density diffuseness along the nuclear surface.

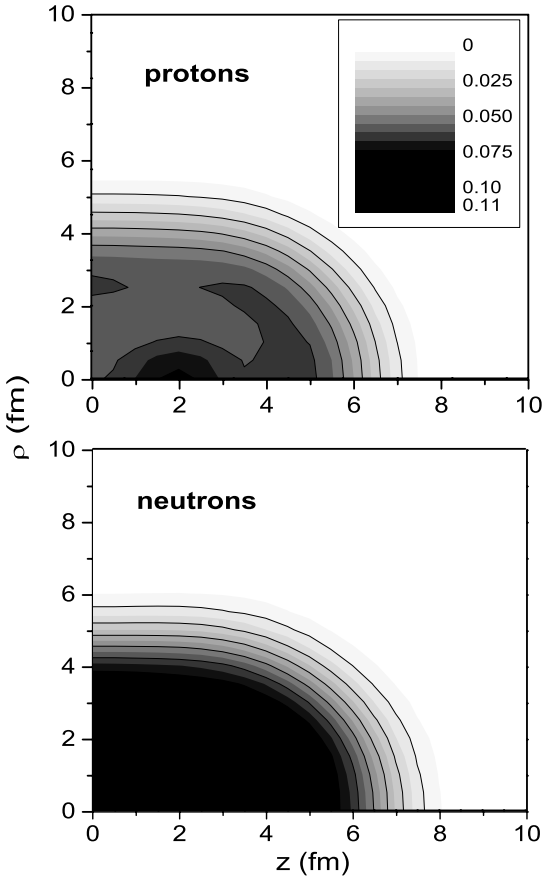

FIG. 5. Contour plots of proton and neutron density distributions in the (ρ, z) plane for the deformed ground state of ^{110}Zr calculated in HFB-AX. The densities are in nucleons/fm^{-3}.

The asymptotic behavior of the nuclear densities depicted in Fig. 6 is consistent with general expectations [10], and the ratio $\rho_n(0, z)/\rho_n(\rho = z, 0)$ is roughly constant at large distances. This indicates that densities are still well deformed in regions well beyond the nuclear surface.

E. Large deformation limit: Axial symmetric fission path of ^{240}Pu

The advantage of coordinate-space calculations over HO expansion methods is apparent in the context of problems involving extreme deformations which require the use of huge oscillator spaces or even a many-center HO basis. In this section, we study the axial, reflection-symmetric fission path of ^{240}Pu, which has been investigated in many earlier works [4]. By carrying out precise HFB-AX calculations, one can assess the error on potential energy surfaces, energies of fission isomers, and fission barriers obtained in commonly used HFB codes employing an HO expansion technique.

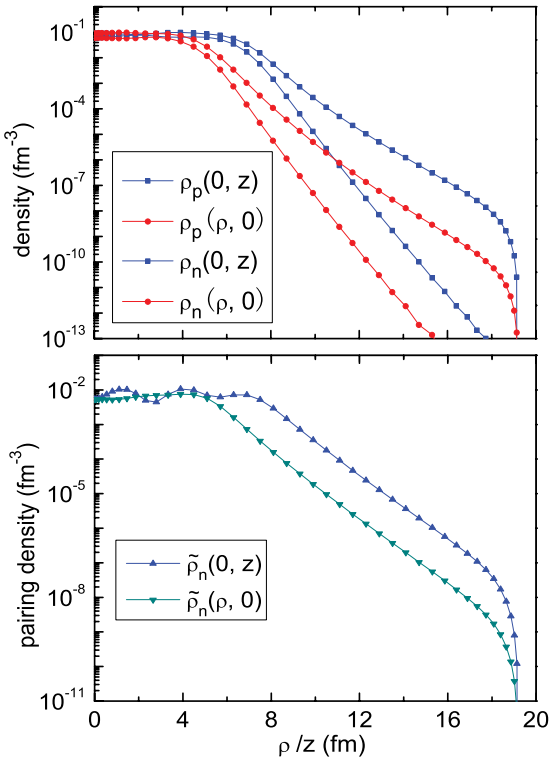

FIG. 6. (Color online) Particle (top) and pairing (bottom) ground-state densities in ^{110}Zr along $\rho = 0$ and $z = 0$. The size of the box is $R = 19.2$ fm.

The HFB energy for a given value of the mass quadrupole moment Q_{20} can be obtained by minimizing the Routhian with a quadratic constraint [7]:

$$E' = E + C_q(\langle\hat{Q}_{20}\rangle - Q_{20})^2, \tag{26}$$

where

$$\langle\hat{Q}_{20}\rangle = 2\pi \int\int \rho_{\rm tot}(\rho, z)(2z^2 - \rho^2)\rho d\rho\, dz \tag{27}$$

is the average value of the mass quadrupole moment, and C_q is the quadrupole stiffness constant.

The constrained HFB-AX calculations for ^{240}Pu were performed in a box of $R = 23.4$ fm and $h = 0.65$ fm, using a B-spline basis with $M = 11$. (For a similar mesh size, the binding energy of ^{120}Sn in HFB-AX agrees with HFBRAD within 50 keV.) The HFBTHO calculations were carried out in a space of $N_{\rm sh} = 20$ spherical or stretched HO shells, which corresponds to an HO basis size typically used in such calculations. The mixed pairing interaction is used with the pairing strength adjusted as in Sec. III B for ^{120}Sn. The results are displayed in Fig. 7. The spherical HO basis is unreliable for fission calculations, and the quality of HFBTHO calculations with a stretched basis deteriorates gradually with deformation. That is, the energy error on the first barrier and fission isomer is ∼100 and ∼400 keV, respectively, and it reaches ∼500 keV inside the second barrier. These are significant corrections that can impact predicted half-lives for spontaneous fission.

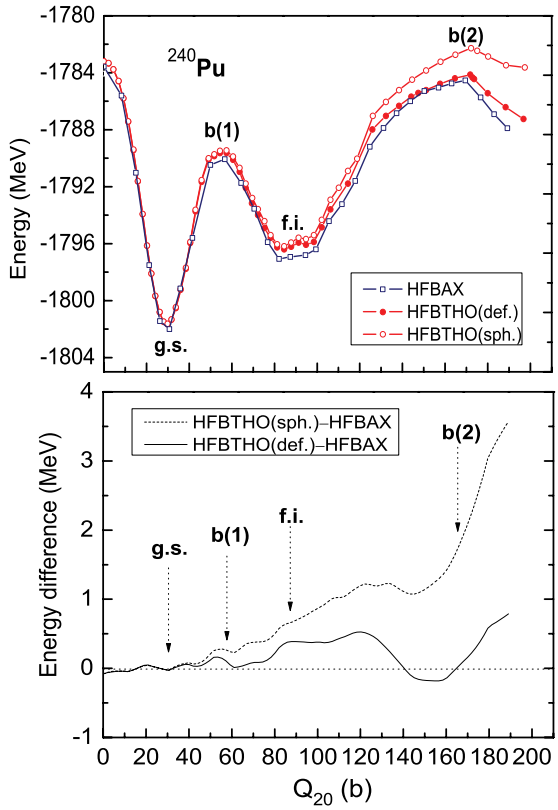

FIG. 7. (Color online) Top: axial, reflection-symmetric fission path of ^{240}Pu calculated with HFB-AX and HFBTHO (in a spherical and stretched HO basis) as a function of the mass quadrupole moment Q_{20} at the self-consistent solution. Bottom: the difference between HFBTHO and HFB-AX results (normalized to zero at the ground-state configuration). The minima and maxima of energy are marked: ground state, g.s.; first barrier, b(1); fission isomer, f.i.; second barrier, b(2).

IV. CONCLUSIONS

We developed the 2D coordinate-space HFB code HFB-AX using the technique of basis splines. The high accuracy of HFB-AX has been demonstrated by comparing its performance with other HFB solvers, both spherical and deformed. The absolute accuracy of the B-splines technique used in HFB-AX has been estimated by comparing with a solver employing the multiresolution wavelet expansion. The ability of HFB-AX to reproduce the salient features of weakly bound nuclei, such as the extended tails of neutron densities in nuclei close to the neutron drip line, has been assessed by using the highly accurate 1D code HFBRAD. Finally, symmetric fission pathways in the heaviest nuclei and deformed halo systems were calculated to compare with the predictions of the deformed configuration-space code HFBTHO.

A significant numerical speedup of the code makes it particularly useful for nuclear structure calculations of exotic configurations, such as nuclear halos and extremely elongated fissioning nuclei, including the superheavy elements. Among the first applications envisioned for HFB-AX are the systematic study of the deformed drip-line nuclei. In this respect, the ability of the code to accommodate very large angular

momentum cutoffs is crucial in the context of nuclei with large neutron excess, for which the high-j continuum has a significant impact on pairing correlations [42].

Other possible applications involve systematic studies of superdeformed configurations and fission isomers. In particular, HFB-AX can provide systematic energy corrections at large deformations, which are essential for the HFB models of nuclear fission based on the HO expansion. The differences seen in Fig. 7 are expected to appreciably impact the predicted spontaneous fission half-lives.

In this work, reflection-asymmetric and triaxial deformations, which are known to be important in realistic fission calculations, have not been investigated. We are currently developing a symmetry-free coordinate-space 3D HFB solver based on the multiresolution wavelet expansion method. The HFB-AX code reported in this paper will provide crucial benchmark tests for this general-purpose, symmetry-unrestricted HFB framework.

ACKNOWLEDGMENTS

This work was supported in part by the US Department of Energy under Contract Nos. DE-FG02-96ER40963 (University of Tennessee), DE-AC05-00OR22725 with UT-Battelle, LLC (Oak Ridge National Laboratory), DE-FG05-87ER40361 (Joint Institute for Heavy Ion Research), and DE-FC02-07ER41457 with UNEDF SciDAC Collaboration. Computational resources were provided by the National Center for Computational Sciences at Oak Ridge and the National Energy Research Scientific Computing Facility.

[1] *RIA Theory Bluebook: A Road Map*, http://www.orau.org/ria/RIATG/Blue_Book_FINAL.pdf.
[2] G. F. Bertsch, D. J. Dean, and W. Nazarewicz, SciDAC Review, Winter 2007, p. 42.
[3] W. Kohn and L. J. Sham, Phys. Rev. A **140**, 1133 (1965).
[4] M. Bender, P.-H. Heenen, and P.-G. Reinhard, Rev. Mod. Phys. **75**, 121 (2003).
[5] *Extended Density Functionals in Nuclear Structure Physics*, edited by G. S. Lalazissis, P. Ring, and D. Vretenar (Springer-Verlag, Berlin, 2004).
[6] E. Perliska, S. G. Rohoziski, J. Dobaczewski, and W. Nazarewicz, Phys. Rev. C **69**, 014316 (2004).
[7] P. Ring and P. Schuck, *The Nuclear Many-Body Problem* (Springer-Verlag, Berlin, 1980).
[8] J. Dobaczewski, M. V. Stoitsov, and W. Nazarewicz, AIP Conf. Proc. **726**, 51 (2004).
[9] J. Dobaczewski, H. Flocard, and J. Treiner, Nucl. Phys. **A422**, 103 (1984).
[10] J. Dobaczewski, W. Nazarewicz, T. R. Werner, J. F. Berger, C. R. Chinn, and J. Dechargé, Phys. Rev. C **53**, 2809 (1996).
[11] V. Blum, G. Lauritsch, J. A. Maruhn, and P.-G. Reinhard, J. Comput. Phys. **100**, 364 (1992).
[12] J. Terasaki, P.-H. Heenen, H. Flocard, and P. Bonche, Nucl. Phys. **A600**, 371 (1996).
[13] P.-H. Heenen, P. Bonche, J. Dobaczewski, H. Flocard, S. J. Krieger, J. Meyer, J. Skalski, N. Tajima, and M. S. Weiss, in *Proceedings of the International Workshop on Nuclear Structure Models*, edited by R. Bengtsson, J. Draayer, and W. Nazarewicz (World Scientific, Singapore, 1992), p. 3.
[14] K. Bennaceur and J. Dobaczewski, Comput. Phys. Commun. **168**, 96 (2005).
[15] E. Terán, V. E. Oberacker, and A. S. Umar, Phys. Rev. C **67**, 064314 (2003).
[16] V. E. Oberacker, A. S. Umar, E. Terán, and A. Blazkiewicz, Phys. Rev. C **68**, 064302 (2003).
[17] A. Blazkiewicz, V. E. Oberacker, A. S. Umar, and M. Stoitsov, Phys. Rev. C **71**, 054321 (2005).
[18] H. Oba and M. Matsuo, Prog. Theor. Phys. **120**, 143 (2008).
[19] P. Bonche, H. Flocard, and P. H. Heenen, Comput. Phys. Commun. **171**, 49 (2005).
[20] N. Tajima, Phys. Rev. C **69**, 034305 (2004).
[21] http://www.csm.ornl.gov/ccsg/html/projects/madness.html.
[22] G. I. Fann, R. J. Harrison, G. Beylkin, J. Jia, R. Hartman-Baker, W. A. Shelton, and S. Sugiki, J. Phys.: Conf. Ser. **78**, 012018 (2007).
[23] M. V. Stoitsov, J. Dobaczewski, W. Nazarewicz, and P. Ring, Comput. Phys. Commun. **167**, 43 (2005).
[24] J. Dobaczewski, W. Nazarewicz, and M. V. Stoitsov, Eur. Phys. J. A **15**, 21 (2002).
[25] J. Dobaczewski, W. Nazarewicz, and P.-G. Reinhard, Nucl. Phys. **A693**, 361 (2001).
[26] http://www.netlib.org/lapack/.
[27] M. Snir, S. Otto, S. Huss-Lederman, D. Walker, and J. Dongarra, *MPI: The Complet Reference* (MIT Press, Cambridge, MA, 1995).
[28] W. H. Press, S. A. Teukolsky, W. T. Vetterling, and B. P. Flannery, *Numerical Recipes in Fortran 77: The Art of Scientific Computing* (Cambridge University Press, Cambridge, England, 1992), p. 480.
[29] D. D. Johnson, Phys. Rev. B **38**, 12807 (1988).
[30] A. Baran, A. Bulgac, M. McNeil Forbes, G. Hagen, W. Nazarewicz, N. Schunck, and M. V. Stoitsov, Phys. Rev. C **78**, 014318 (2008).
[31] E. Chabanat, P. Bonche, P. Haensel, J. Meyer, and R. Schaeffer, Nucl. Phys. **A635**, 231 (1998).
[32] R. J. Harrison, G. I. Fann, T. Yanai, Z. Gan, and G. Beylkin, J. Chem. Phys. **121**, 11587 (2004).
[33] J. A. Maruhn and W. Greiner, Z. Phys. **251**, 431 (1972).
[34] M. Marini, F. Pistolesi, and G. C. Strinati, Eur. Phys. J. B **1**, 151 (1998).
[35] T. Papenbrock and G. F. Bertsch, Phys. Rev. C **59**, 2052 (1999).
[36] P. J. Borycki, J. Dobaczewski, W. Nazarewicz, and M. V. Stoitsov Phys. Rev. C **73**, 044319 (2006).
[37] J. Meng and P. Ring, Phys. Rev. Lett. **77**, 3963 (1996).
[38] K. Bennaceur, J. Dobaczewski, and M. Płoszajczak, Phys. Lett. **B496**, 154 (2000).
[39] J. Terasaki and J. Engel, Phys. Rev. C **76**, 044320 (2007).
[40] J. Margueron, H. Sagawa, and K. Hagino, Phys. Rev. C **77**, 054309 (2008).
[41] M. Stoitsov, N. Michel, and K. Matsuyanagi, Phys. Rev. C **77**, 054301 (2008).
[42] V. Rotival, K. Bennaceur, and T. Duguet, arXiv:0711.1275; V. Rotival and T. Duguet, arXiv:nucl-th/0702050.